Science Advances

AAAS

advances.sciencemag.org/cgi/content/full/2/11/e1601661/DC1

Supplementary Materials for

Helical and rod-shaped bacteria swim in helical trajectories with little additional propulsion from helical shape

Maira A. Constantino, Mehdi Jabbarzadeh, Henry C. Fu, Rama Bansil

Published 16 November 2016, *Sci. Adv.* **2**, e1601661 (2016)
DOI: 10.1126/sciadv.1601661

The PDF file includes:

- Legends for movies S1 to S5
- fig. S1. Head and flagellar junction trajectories of LSH100 helical *H. pylori* swimming in PGM (15 mg/ml) (movie S1).
- fig. S2. Swimming speed versus axial length, calculated by decoupled model.
- fig. S3. Swimming power versus axial length for right- and left-handed helical cells and rod-shaped cell body.
- Numerical calculation methods
- References (*60*, *61*)

Other Supplementary Material for this manuscript includes the following:
(available at advances.sciencemag.org/cgi/content/full/2/11/e1601661/DC1)

- movie S1 (.mov format). Motility of LSH100 WT (helical) *H. pylori* swimming in PGM (15 mg/ml) imaged with 100× lens, 200 fps.
- movie S2 (.mov format). Flagellar bundle visualization.
- movie S3 (.mov format). Motility of LSH100 Δ*csd6* (rod mutant) *H. pylori* swimming in PGM (15 mg/ml) imaged with 100× lens, 100 fps.
- movie S4 (.mov format). Motility of LSH100 WT (helical) *H. pylori* swimming in BB10 imaged with 100× lens, 200 fps.
- movie S5 (.mov format). Motility of LSH100 Δ*csd6* (rod mutant) *H. pylori* swimming in BB10 imaged with 40× lens, 30 fps.

Supplementary Materials

movie S1. Motility of LSH100 WT (helical) *H. pylori* swimming in PGM (15 mg/ml) imaged with 100× lens, 200 fps.

movie S2. Flagellar bundle visualization. This is movie S1 with increased contrast.

movie S3. Motility of LSH100 Δ*csd6* (rod mutant) *H. pylori* swimming in PGM (15 mg/ml) imaged with 100× lens, 100 fps.

movie S4. Motility of LSH100 WT (helical) *H. pylori* swimming in BB10 imaged with 100× lens, 200 fps. Flagellar junction can be identified as more rapid changes in contrast at one end than the other during the time interval 2.500s to 2.700s. The end with the more rapid change in contrast is identified as the flagellar junction, and in some frames a very faint outline of flagella can be seen.

movie S5. Motility of LSH100 Δ*csd6* (rod mutant) *H. pylori* swimming in BB10 imaged with 40× lens, 30 fps. Flagellar junction can be identified as more rapid changes in contrast at one end than the other during the time interval 0.198s to 1.089s.

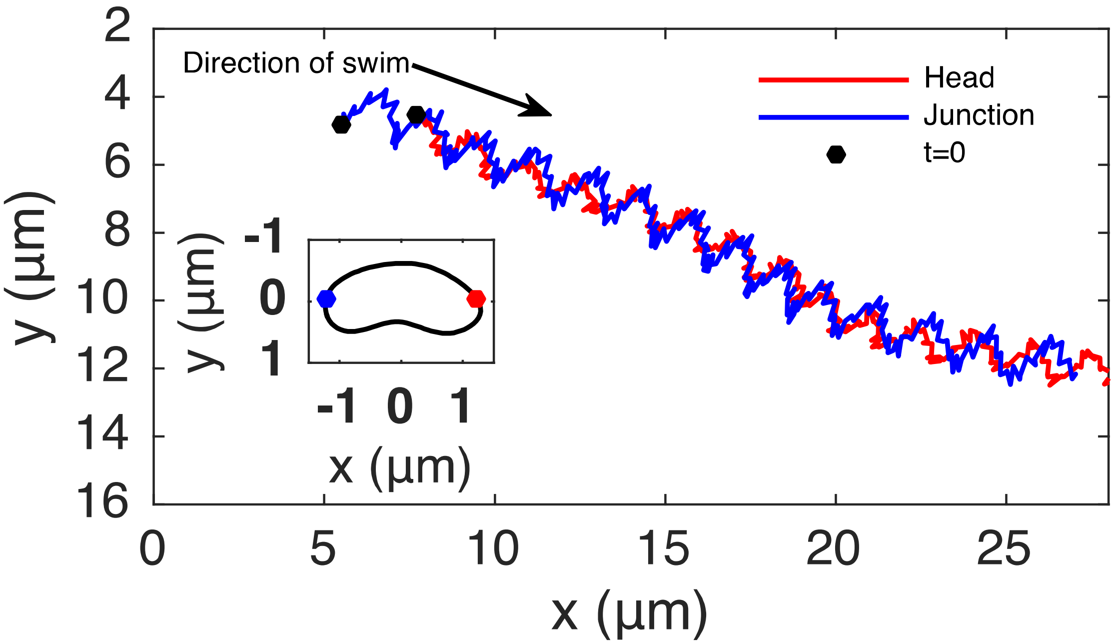

fig. S1. Head and flagellar junction trajectories of LSH100 helical *H. pylori* swimming in PGM (15 mg/ml) (movie S1). Red line is the trajectory of head point and blue line of the flagellar junction point. The trajectory pitch was obtained for both head and flagellar junction trajectories by de-trending the trajectories and measuring the distance between peaks for the entire track. As expected, the head and flagellar junction pitches are the same, $P_T = 1.5 \pm 0.2$ µm (the pitch is the average of the entire run and the error is the standard deviation). The trajectory radius is obtained by measuring the distance between the top and bottom envelope functions, $R_{head} = 0.45 \pm 0.03$ µm, $R_{junction} = 0.55 \pm 0.06$ µm (the radius is the average of the entire run and the error is the standard deviation). Inset: Example of definition of head and flagellar junction points. The head and flagellar junction points have to be defined for every frame because there is not a marker or feature in the bacterium's images. The contour of the body (in black) was aligned and centered with CellTool [36]. The head (red) and flagellar junction points (blue) were defined as the contour points intercepting the line y = 0. CellTool [36] saves the original alignment angle and localization of center point thus the trajectory can be reconstructed.

Numerical calculation methods

Regularized Stokeslets. To investigate the swimming properties of a helical cell body driven by rotating helical flagella, we use the method of regularized Stokeslets (RSM) [46, 47]. The flagellar bundle is modeled as a single helical flagellum, so for convenience we refer to it as the flagellum in the rest of the Supplementary Materials. In this method the surface of the cell body and flagellum is discretized by regularized Stokeslets which are fundamental solutions to the Stokes equation for applied localized force distributions $\phi_{\epsilon}(\mathbf{r}) = 15\epsilon^4\mathbf{f}/\left[8\pi(r^2+\epsilon^2)^{7/2}\right]$ that are smooth approximation for delta function. The small parameter ϵ controls the size of the distribution. The total flow velocity is

$$\mathbf{v}(\mathbf{r}) = \sum_{j=1}^{N} \mathbf{S}\left(\mathbf{r}-\mathbf{r}_j\right)\mathbf{f}_j \tag{1}$$

where **f** is the vector of localized force of each regularized Stokeslet, **r** is the position at which velocity is being calculated $\mathbf{r}_j$ is the position of the Stokeslet, and $S_{ij}(\mathbf{x}) = \frac{1}{8\pi\mu}\left(\frac{\delta_{ij}(x^2+2\epsilon^2)+x_ix_j}{(x^2+\epsilon^2)^{\frac{3}{2}}}\right)$ is the regularized Stokeslet which depends on cutoff parameter ϵ.

To solve equation (1), we need to find localized forces of Stokeslets on the surface of the cell and flagellum. Using no-slip boundary conditions on the surface it is convenient to express the velocity at each point of the surface to the swimming velocity and rotation in body-fixed-frame of the swimmer. This relation can be written as

$$\mathbf{v}(\mathbf{r_j}) = \mathbf{V} + \mathbf{\Omega} \times \mathbf{r_j} + \dot{\mathbf{L}}_\mathbf{j} \tag{2}$$

where $\mathbf{V}$ and $\mathbf{\Omega}$ are swimming velocity and rotation vector respectively, $\mathbf{r_j}$ are the Stokeslet positions placed on material points of the surfaces in the body-fixed-frame, and $\dot{\mathbf{L}}_\mathbf{j}$ are the velocity of the Stokeslets with respect to the body-fixed-frame. In our case, the flagellum is rotating relative to the cell body with relative rotational velocity of $\mathbf{\Omega}$, so $\mathbf{r_j}$ is fixed for the positions on the cell body, but rotates for the flagellum. Thus $\dot{\mathbf{L}}_\mathbf{j}$ is the rotational velocity ($\dot{\mathbf{L}}_\mathbf{j} = \mathbf{\Omega} \times \mathbf{r_j}$) of the flagellum and zero for the cell body. To find the six unknowns (components of velocity and rotation of the swimmer) in equation (2), we apply zero total force and torque conditions for a free swimmer in the fluid, $\sum_j \mathbf{f_j} = 0$, and $\sum_j \mathbf{r_j} \times \mathbf{f_j} = 0$, which yields a linear system of equations in the body-fixed-frame that can be solved at each time step of flagellum rotation.

We use as the origin of the body-fixed-frame the junction point of the body and flagellum, with x-axis along the center-line of the flagellum (Fig. 1). The flagellum rotates along this axis with constant rotational velocity $\mathbf{\Omega}$. Similar to work done by Hyon et al. [37], we only solve for one rotation of flagellum and record velocities and rotations in the local frame, because after one full rotation of the flagellum in the local frame its position with respect to the cell body will be same as the initial state and we can use results for first rotation of the flagellum to reproduce results for many other revolutions. By converting these data to the lab frame and integrating velocities we find the position of the swimmer in the lab frame, which traces a helical trajectory. Unless otherwise specified, we report the average swimming speed, which is the component of the instantaneous velocity along the direction of the rotation, $V_s = \mathbf{V}.\hat{\mathbf{\Omega}}_b$.

Geometry used in calculations. The cell body is modeled as a standard helix with its centerline positions given by

$$\mathbf{r}(x) = x\hat{\mathbf{x}} + R_B \cos(kx)\,\hat{\mathbf{y}} + R_B \sin(kx)\,\hat{\mathbf{z}} \tag{3}$$

where $k = 2\pi/P_B$ is the wave number, R_B is the helical radius and P_B is the pitch of the cell body. The surface of the helix can be represented by the coordinates $(x + H(x,\phi), R_B\cos(kx) + M(x,\phi), R_B\sin(kx) + N(x,\phi))$ where $0 \le \phi \le 2\pi$ is the polar coordinate for the body's cross section orthogonal to the center-line at point x and H, M and N are some functions of x and ϕ [60]. We discretize the helical surface by choosing points at intervals Δx and $\Delta\phi$ in x and ϕ, respectively, such that the spacing between points (ΔS_b) for the cross section and longitudinal directions of the helix is uniform. We also use two hemispherical caps for the ends of the helix to generate a closed body. To discretize the caps, we try to keep uniform spacing in circular cross sections and radial direction of the hemispheres close to the cell body spacing ΔS_b. For the cell body geometry, we use the mean values for the pitch and helical radius while varying axial length, or mean values for the helical radius and axial length while varying pitch. The mean values are obtained from histogram of helical parameters previously obtained by Martinez et al. [28] using the cell outline software CellTool [36].

H. Pylori has multiple flagella at one end that bundle form a flagellar bundle during propulsion. In our model we treat this flagellar bundle as a single helix. We taper the bundle's helical radius near the cell body [60, 61] and assume the centerline of the bundle is along the **x** axis so the equation of the centerline could be described by

$$\mathbf{r}(\mathrm{x}) = \mathrm{x}\hat{\mathbf{x}} + \left(1 - \mathrm{e}^{-\left(\mathrm{x}/\mathrm{k_e}\right)^2}\right)\mathrm{R}\left(\cos\left(\frac{2\pi}{\mathrm{P}}\,\mathrm{x}\right)\hat{\mathbf{y}} + \sin\left(\frac{2\pi}{\mathrm{P}}\,\mathrm{x}\right)\hat{\mathbf{z}}\right) \tag{4}$$

Here P is the pitch of the bundle and k_e is the characteristic length of the tapering region and considered to be equal to $k_e = P/2\pi$. To discretize the bundle surface, we first a discretize circular cross section with spacing ΔS_f then sweep along the center-line creating discretized cross sections at the same spacing to place points on the entire surface. Finally, we add two discretized hemispherical caps to the ends of the flagellum. The helical properties of the flagellum are given in Table (2).

Satisfying observed body rotation or constant torque constraints. The calculations are performed by prescribing a constant angular velocity of the flagellum relative to the cell body. Given this relative rotation rate, both the cell body and flagellum rotation rate relative to the lab frame are determined by torque balance. All three rotation rates are proportional to each other as well as to the swimming velocities. To achieve an observed body rotation rate, we scale all the rotation rates and velocities by the same amount. Equivalently, we can present the calculated swimming speed result as the ratio V/Ω_b as in Table 1. For comparisons of swimming speeds between different cell body geometries, it is more realistic to consider that the flagellar motor is likely operating in the constant-torque regime of its angular velocity-torque curve. Thus, to present results for constant flagellar torque, all the results reported here are nondimensionalized using the flagellar torque, which can be obtained from the forces and positions of the regularized Stokeslets.

Convergence. We performed convergence tests using regularized Stokeslets to validate the results. More Stokeslets on the surface results in more accuracy, but at the cost of computational efficiency. So we aim to use a reasonable number of Stokeslets to reduce costs while achieving acceptable accuracy for calculations. In our convergence tests, we separately discretize the body and flagellum with different number of Stokeslets on each surface (N_{body}, $N_{flagella}$, respectively). We checked that swimming speeds converged as N_{body}, $N_{flagella}$ are increased. In the reported results, we use $N_{flagella} = 4312$ and N_{body} about 2000, for which the difference in results from our most accurate calculations using the largest numbers of Stokeslets is about 1.4%.

Estimates of cell-body and flagellar thrust from a hydrodynamically decoupled model. In this model, we calculate resistance matrices for the head and flagellum separately using the RSM. The force and torque on the body ($\mathbf{F_b}$ and $\mathbf{N_b}$) and flagellum ($\mathbf{F_f}$ and $\mathbf{N_f}$) are expressed in terms of the resistance matrices as

$$\begin{pmatrix} \mathbf{F_f} \\ \mathbf{N_f} \end{pmatrix} = \mathbf{R}_\mathrm{f} \begin{pmatrix} \mathbf{V} \\ \mathbf{\Omega}_\mathrm{f} \end{pmatrix} \tag{5}$$

$$\begin{pmatrix} \mathbf{F_b} \\ \mathbf{N_b} \end{pmatrix} = \mathbf{R}_\mathrm{b} \begin{pmatrix} \mathbf{V} \\ \mathbf{\Omega}_\mathrm{b} \end{pmatrix} \tag{6}$$

The origin for the resistance matrices is chosen to be the attachment point of the flagellum on the cell body, so $\mathbf{V}$ is the translational velocity of the attachment point, and $\mathbf{\Omega_b}$ and $\mathbf{\Omega_f}$ are the angular velocities of the cell body and flagellum, respectively, about the attachment point. Total hydrodynamic forces and torques are calculated by summing the forces and torques resulting from these resistance matrices

$$\begin{pmatrix} \mathbf{F} \\ \mathbf{N} \end{pmatrix} = \mathbf{R_b} \begin{pmatrix} \mathbf{V} \\ \mathbf{\Omega_b} \end{pmatrix} + \mathbf{R_f} \begin{pmatrix} \mathbf{V} \\ \mathbf{\Omega_b} + \mathbf{\Omega} \end{pmatrix} \tag{7}$$

which ignores interactions between the flagellum and cell body. Applying the constant relative rotation rate between the flagellum and body yields $\mathbf{\Omega}_\mathrm{f} = \mathbf{\Omega}_\mathrm{b} + \mathbf{\Omega}$, and by enforcing the force- and torque-free constraints for the swimmer, we calculate the instantaneous velocity and body rotation rate

$$\begin{pmatrix} \mathbf{V} \\ \mathbf{\Omega}_\mathrm{b} \end{pmatrix} = -(\mathbf{R}_\mathrm{f} + \mathbf{R}_\mathrm{b})^{-1} \mathbf{R}_\mathrm{f} \begin{pmatrix} \mathbf{0} \\ \mathbf{\Omega} \end{pmatrix} \tag{8}$$

As in the numerical calculations, the average swimming velocity is $\mathrm{V}_\mathrm{s} = \mathbf{V}.\hat{\mathbf{\Omega}}_\mathrm{b}$. To assess the accuracy of this model, we first compare the swimming velocity calculated by the decoupled model to the numerical results including all hydrodynamic interactions previously presented in Figure 3A. Figure S2 shows the swimming speeds as a function of axial length for all three scenarios presented in Figure 3A, while the inset shows the error in swimming speed relative to the results of Figure 3A. The trends in swimming speeds are similar, and the decoupled model is within 20% accuracy for shorter helical cell bodies (axial length < 1 μm), and always within 30% for the biological scenario of a right-handed cell body. Thus, although the decoupled model is not quantitatively accurate it is likely to capture the qualitative trends in swimming speeds.

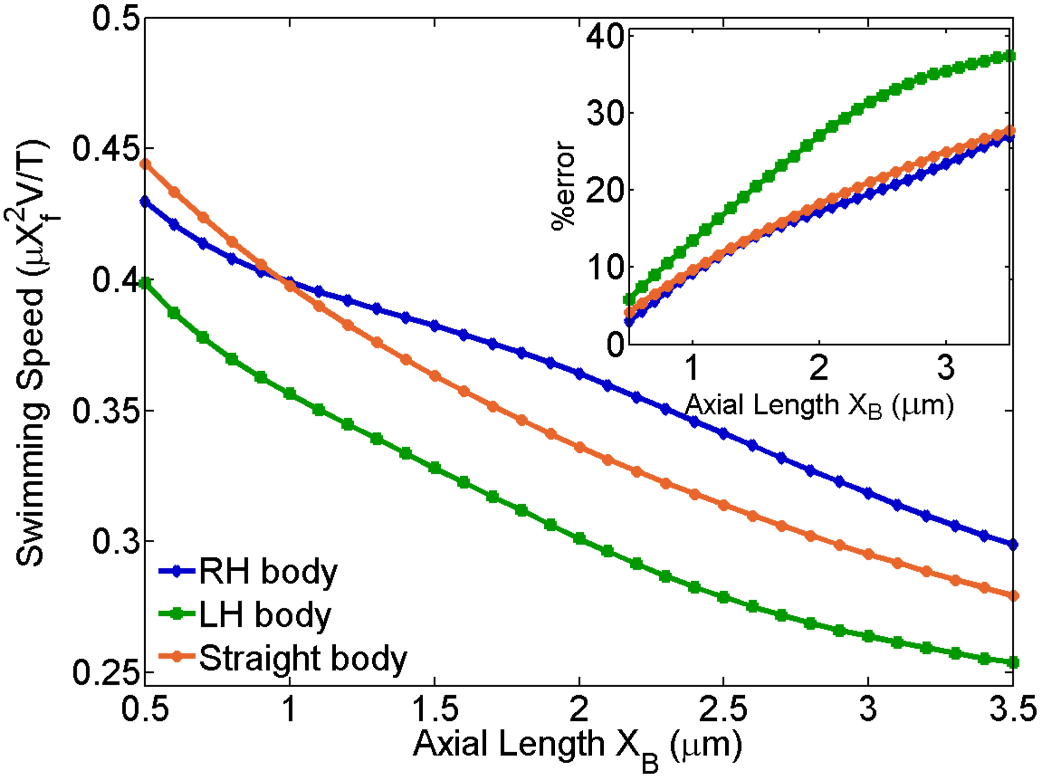

fig. S2. Swimming speed versus axial length, calculated by decoupled model. Comparison to the results of Fig. 3A reveals the accuracy of the decoupled model. Inset: Percent error of the decoupled model relative to the results of Fig. 3A.

Using the decoupled model, it is possible to estimate the total drag (D_T), and the thrust from the cell body (T_b) and flagellum (T_f) separately

$$\mathbf{D_T} = (\mathbf{R}_b + \mathbf{R}_f)\begin{pmatrix}\mathbf{V}\\ \mathbf{0}\end{pmatrix} \tag{9}$$

$$\mathbf{T_b} = \mathbf{R}_b\begin{pmatrix}\mathbf{0}\\ \mathbf{\Omega}_b\end{pmatrix} \tag{10}$$

$$\mathbf{T_f} = \mathbf{R}_f\begin{pmatrix}\mathbf{0}\\ \mathbf{\Omega}_b + \mathbf{\Omega}\end{pmatrix} \tag{11}$$

Power and efficiency. Figure S3 shows the power ($\mathrm{P} = \mathrm{N}\,\boldsymbol{\Omega}$) expended by the bacterial geometries explored in Fig. 3A. Note the scale of the vertical axis implies that the helicity of the body has little (<3%) effect on power expended. From the power, we can calculate the swimming efficiency

$$\eta = \frac{\mathrm{V}^2 \mathrm{R}_{\mathrm{trans}}}{\mathrm{P}} \tag{12}$$

where P is the total power, and V and $\mathrm{R}_{\mathrm{trans}}$ are the swimming velocity and translational resistance of the cell body in the swimming direction. The resulting efficiency for the geometries in Fig. 3A are shown in the inset to fig. S3. Comparing the left-handed, right-handed and rod-shaped cell bodies at any fixed axial length, and keeping in mind that the power is little affected by the cell body geometry (fig. S3), we find that most of the change in swimming efficiency is accounted for by the corresponding difference in swimming velocities in Fig. 3A; for example, if the right-handed body is 10% faster than the straight body, then the efficiency is approximately a factor of $1.21 = 1.1^2$ higher.

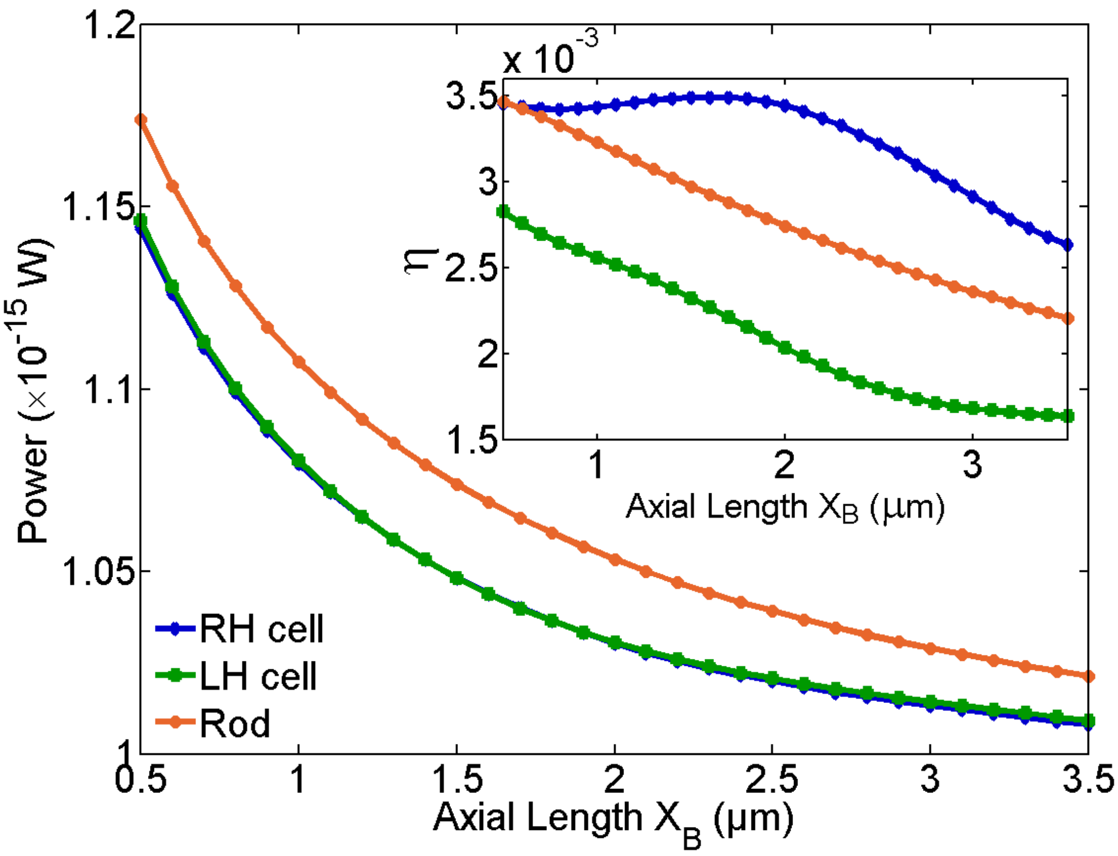

fig. S3. Swimming power versus axial length for right- and left-handed helical cells and rod-shaped cell body. Inset: Swimming efficiency vs axial length for RH and LH helical cells and rod-shaped cell body.